Showcasing research from the group of Prof. Adlane Sayede at Unit of Catalysis and Solid Chemistry (UCCS), Artois University, France.

Enhancing the electronic and photocatalytic properties of $(SnO_2)_n/(TiO_2)_m$ oxide superlattices for efficient hydrogen production: a first-principles study

This study explores the structural, electronic, and photocatalytic properties of $(SnO_2)_n/(TiO_2)_m$ superlattices using density functional theory. Biaxial strain enables tuneable band gaps, enhanced stability, and favourable band edge alignments with water redox potentials. Tensile strain notably boosts photocatalytic efficiency, making these materials promising for hydrogen production *via* water splitting. The findings provide insights into designing advanced photocatalysts for renewable energy, paving the way for more efficient solar-to-chemical energy conversion.

As featured in:

ROYAL SOCIETY OF CHEMISTRY

rsc.li/pccp

PCCP
Owner Societies

Check for updates

Enhancing the electronic and photocatalytic properties of $(SnO_2)_n/(TiO_2)_m$ oxide superlattices for efficient hydrogen production: a first-principles study†

Najwa Harrati,* Bastien Casier and Adlane Sayede ᴰ *

The effects of biaxial tensile and compressive strain on the structural, electronic, and photocatalytic properties of tetragonal [001] $(SnO_2)_n/(TiO_2)_m$ superlattices have been theoretically explored using density functional theory (DFT) calculations. Various stacking periodicities between n SnO_2 layers and m TiO_2 layers, including ($n = m$), (n, 1), and (1, m) were studied in the context of water splitting for hydrogen production. The results reveal that the (1, m) stacking periodicity exhibit the highest bulk modulus, Poisson's ratio, and Debye temperature values. Phonon dispersion analysis showed excellent stability for the $(SnO_2)_3/(TiO_2)_1$ superlattice under both tensile and compressive strains ranging from -5% to 5%, while other superlattices remain stable within the range of -3% to 4%. Furthermore, the electronic analysis revealed a decreasing trend in the band gap for all structures as the tensile strain increases. A tunable band gap from 3.34 eV to 2.54 eV under tensile strains for $(SnO_2)_1/(TiO_2)_3$ was found using the HSE06 functional, exhibiting high carrier mobility. Favorable band edge alignments at pH 0, 7, and 14 highlight the potential of these superlattices as efficient photocatalysts. The results demonstrate that applying tensile strain to $(SnO_2)_n/(TiO_2)_m$ superlattices with high TiO_2 thickness can result in optimal band gap values and favorable band edge alignments with the water redox potentials. This makes these superlattices promising for hydrogen production from water splitting.

1. Introduction

As industrial and societal advancements continue, public attention has increasingly focused on concerns surrounding energy shortages and environmental pollution. One potential solution to tackle this challenge involves the conversion of low-density solar energy into high-density chemical energy through the use of photocatalytic technology, which does not emit greenhouse gases. In this regard, the production of hydrogen from water splitting has been demonstrated as a promising technology for harvesting solar energy, one of the most abundant energy sources available on Earth.[1] In general, the performance of photocatalytic processes hinges on three key factors: the characteristics of the used photo-catalytic material, particularly its bandgap energy and band edge positions; the spectrum of light irradiation; and the dynamics of interfacial charge transfer occurring at its surface. In this context, superlattices are becoming increasingly widespread in the photocatalytic field.[2–4] They exhibit notable functionalities, including the customization of band gaps, the facilitation of spatial charge separation across various interfaces, the mitigation of charge carriers recombination, and adjustment of absorption spectra towards the visible spectrum.[5,6]

Transition metal oxides have been extensively investigated for their excellent stability and photocatalytic properties.[7,8] Among the studied materials, considerable interest has been focused on the binary compounds XO_2 (X: Ti and Sn) owing to their chemical and physical characteristics exhibited in the rutile phases (space group no. 136; D_{4h}^{14}; $P4_2/mnm$). TiO_2 is considered the most intensively used and studied photocatalyst semiconductor, combining several optimistic features, including non-toxic environmental acceptability, low cost, and excellent stability against photo-corrosion.[9,10] However, the high recombination of photo-generated charge carriers remains a significant challenge to overall efficiency.[11,12] Indeed, SnO_2 exhibits superior electron mobility and high electron transfer efficiency,[13] thereby preventing rapid electron/hole recombination, but the conduction band minimum (CBM) positioned above the redox potential level of H^+/H_2 (0 eV) presents a complication that restricts its widespread

Univ. Artois, CNRS, Centrale Lille, Univ. Lille, UMR 8181, Unité de Catalyse et de Chimie du Solide (UCCS), F-62300 Lens, France.
E-mail: adlane.sayede@univ-artois.fr, najwa.harrati@univ-artois.fr
† Electronic supplementary information (ESI) available. See DOI: https://doi.org/10.1039/d4cp03363a

application as a photo-catalyst for the hydrogen evolution reaction (HER).[14] Moreover, these materials have wide direct band gap energies (TiO$_2$, E_g = 3.1–3.3 eV; SnO$_2$, E_g = 3.6 eV) that limit their absorption under UV irradiation, allowing them to use only 3–5% of the solar spectrum. Nowadays, several experimental and theoretical investigations have demonstrated the potential for strain induced alteration or adjustment of the band gap in TiO$_2$ and SnO$_2$ materials.[15,16] For example, the effect of biaxial strain applied to the *bc* plane of SnO$_2$ has been investigated experimentally and theoretically on Al$_2$O$_3$ substrates with the HSE06 approximation by Wei Zhou.[17] Their results pointed out that the optical band gap reduces by 0.7 eV with increasing tensile strain. There are limited studies on SnO$_2$/TiO$_2$ superlattice, and those which do exist are focused on the photocatalytic performance for degradation of methyl blue dye under UV irradiation. Recently, experimental study on SnO$_2$/TiO$_2$ heterostructures with anatase TiO$_2$ and kesterite SnO$_2$ phases proved that the energy band gap of TiO$_2$ and SnO$_2$ in the heterojunction have lower energy band gap compared to their individual metal oxides.[18] However, theoretical investigations on such superlattices under strain effects are still limited, and thus there is a lot yet to be explored regarding biaxial strain in the *ab* plane.

In the present study, the effect of biaxial tensile and compressive strains on the photoelectrochemical properties of (SnO$_2$)$_{(n)}$/(TiO$_2$)$_{(m)}$ superlattices, obtained by stacking n layers of SnO$_2$ with m layers of TiO$_2$ (n and m = 1, 2, 3), was investigated using *ab initio* density functional theory (DFT) calculations. Our primary focus was to investigate the effects of n/m thickness periodicity along the [001] direction on the dynamics, mechanical stability, lattice geometry, electronic, mechanical and photocatalytic properties of (SnO$_2$)$_{(n)}$/(TiO$_2$)$_{(m)}$ superlattices. In addition, our secondary objective was to investigate the influence of biaxial tensile and compressive strains ranging from −5% to 5% with a step of 1% on the said properties of these superlattices.

2. Computational details

The influence of the biaxial tensile and compressive strains on a set of (SnO$_2$)$_{(n)}$/(TiO$_2$)$_{(m)}$ [nSO/mTO] superlattices were investigated using DFT calculations.[19,20] Various arrangements involving the stacking of n unit cells of SnO$_2$ (SO) with m unit cells of TiO$_2$ (TO) (n, m = 1, 2, 3) were explored, resulting in diverse combinations of nSO/mTO layers.

The studied structures are presented in Fig. 1, the biaxial strain was considered from −5% (4.430 Å) to 5% (4.900 Å) and was defined as:

$$\varepsilon\,(\%) = \frac{a - a_0}{a_0} \times 100, \qquad (1)$$

where a_0 (4.664 Å) and a are the lattice parameters for unstrained and strained structures, respectively. Negative values correspond to compressive strain, while positive values indicate tensile strain. The value of a_0 is derived for an average of the optimised lattice parameters of SnO$_2$ and TiO$_2$, which

exhibit a mismatch of ±1.5%. All calculations were performed within the DFT framework, using the Vienna *Ab initio* Simulation Package (VASP).[21–23] The all-electron plane wave basis sets with the projector augmented wave (PAW) method have been adopted, with 5s^{2}5p^2, 3p^{6}3d^{2}4s^2, and 2s^{2}2p^4 states treated as valence electrons for Sn, Ti, and O, respectively. To solve the DFT Kohn–Sham equations along the structure relaxations, the generalized gradient approximation (GGA) defined through the Perdew–Burke–Ernzerhof (PBE) parameters functional was adopted.[24] To achieve optimal accuracy in the computed results, the energy cutoff was set at 800 eV, and the Brillouin zone (BZ) was sampled using a 4 × 4 × 6 Monkhorst–Pack k-point mesh.[25] Convergence in the self-consistent field calculations was ensured by setting the thresholds, for total energy and forces, to 10^{-7} eV and 10^{-3} eV Å^{-1}, respectively. To address the limitations of DFT-GGA in estimating band gaps, we adopted the Heyd–Scuseria–Ernzerhof hybrid functional (HSE06) with 25% exact Hartree–Fock exchange to enhance the accuracy of electronic property computations.[26] Phonon dispersion curves and the associated phonon density of states (PhDOS) were determined using the Phonopy software,[27] in conjunction with VASP *via* Density Functional Perturbation Theory (DFPT). For the treatment of the highly correlated Ti-3 d electrons, the Hubbard Correction (DFT+U) approach was used,[28] following the methodology by Dudarev *et al.*,[29] with an effective Hubbard U_{eff} value of 4.5 eV. The analysis of VASP-generated data was conducted using the VASPKIT tool,[30] and visualization was performed with VESTA software.[31]

3. Results and discussion

3.1. Structural properties of the superlattices

Initially, a fully structural relaxation was performed for both rutile phases of SnO$_2$ and TiO$_2$, which have served as building blocks of our superlattices. The lattice parameters obtained for both SnO$_2$ and TiO$_2$ were found to be in good agreement with experimental values, as shown in Table S1 (referred in the ESI†).

The optimization of both unstrained and strained superlattice structures was carried out at the same theoretical level. For each system, varying levels of biaxial strain were applied to explore the impact on total energy with changes in the out-of-plane lattice parameter c. The stability of the structures was assessed by analyzing the total energy as a function of volume $E(V)$ across seven superlattices, as shown in Fig. 1. The equilibrium parameter c and volume were ascertained by fitting data to the Birch–Murnaghan third-order equation of state (EOS).[32] As an example, Fig. 2 illustrates the energy curves $E\left(\dfrac{c}{a}\right)$ and $E(V)$ for the 1SO/1TO superlattice under both tensile and compressive strains, highlighting the sensitivity of superlattice stability to tetragonal distortion. Detailed results for additional superlattices are presented in the ESI† (Fig. S1–S3).

The calculated lattice parameters and bond angles of unstrained superlattices are presented in Table 1. From this table, it was found that the out of plane lattice constant c_0, and
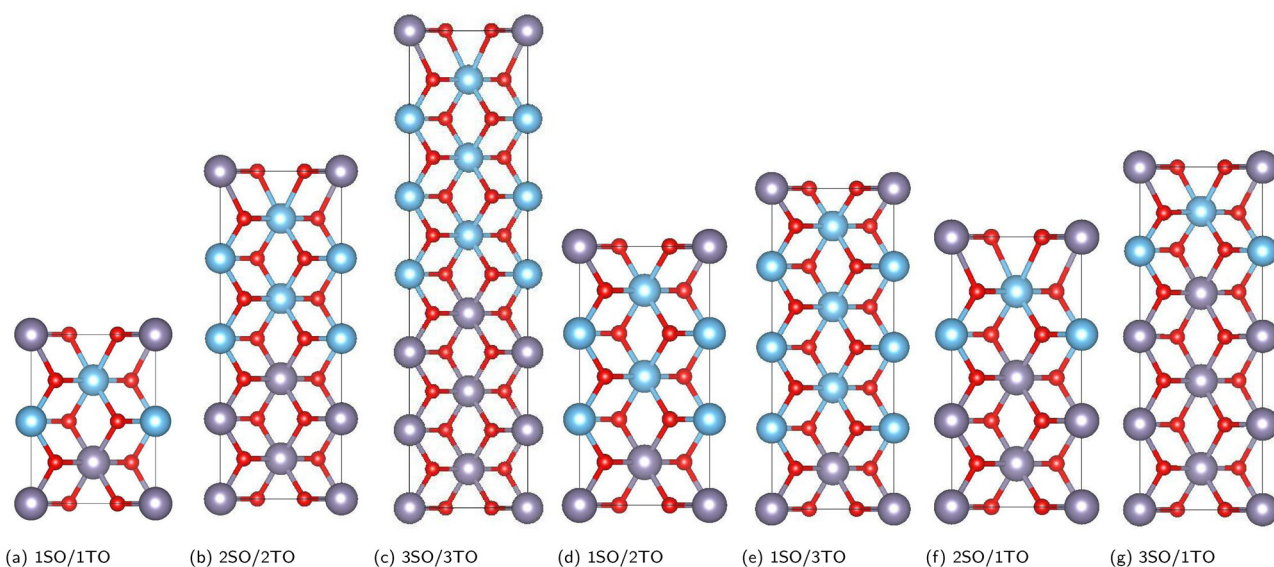
This journal is © the Owner Societies 2025

Phys. Chem. Chem. Phys., 2025, **27**, 1284–1297 | 1285

Fig. 1 (a)–(g) Schematic view of $(SnO_2)_{(n)}/(TiO_2)_{(m)}$ (n,m = 1, 2, 3) superlattices, where n and m are the number of unit cells of SnO_2 (SO) and TiO_2 (TO), respectively (gray, blue, and red colors represent Sn, Ti, and O atoms).

its ratio $\frac{c_0}{a_0}$, increase with increasing SnO_2 layers and decrease with increasing TiO_2 layers. Furthermore, it is observed that both c_0 and $\frac{c_0}{a_0}$ decrease when the number of layers of both SnO_2 and TiO_2 increases simultaneously. The $\frac{c_0}{a_0}$ ratio reflects the
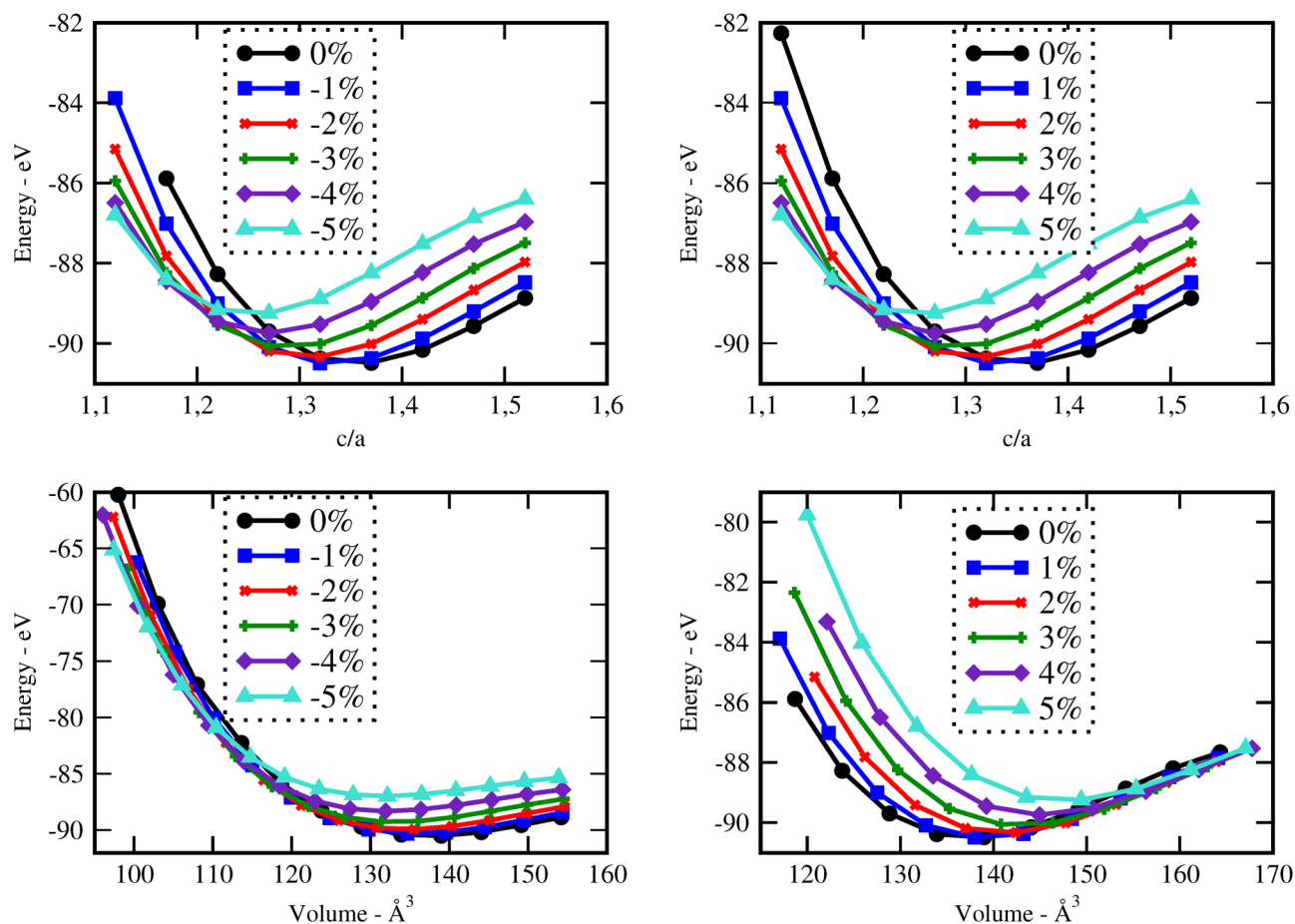

Fig. 2 Structure stability of the 1SO/1TO superlattice under compressive (left) and tensile (right) strains.

1286 | *Phys. Chem. Chem. Phys.*, 2025, **27**, 1284–1297

This journal is © the Owner Societies 2025

Table 1 Lattice parameters and bond angles of unstrained nSO/mTO superlattices (the values of c_0, $\frac{c_0}{a_0}$, and angles are the average values of overall superlattices)

$\varepsilon = 0\%$	Lattice parameters		Angles (°)	
	c (Å)	$\frac{c_0}{a_0}$	O–Sn–O	O–Ti–O
1SO/1TO	3.1655	0.67873	88.1401	90.1874
2SO/2TO	3.1515	0.67574	88.7057	90.7862
3SO/3TO	3.1480	0.67499	88.6243	90.3675
1SO/2TO	3.0925	0.66309	87.9621	89.9074
1SO/3TO	3.0557	0.65519	87.8890	89.8069
2SO/1TO	3.2150	0.68937	88.6952	90.6707
3SO/1TO	3.2450	0.69579	88.8401	90.7874

tetragonal distortion, the observed increase of this ratio indicates an augmentation of relative displacement between cations and anions. Comparing the bond angles O–Sn–O and O–Ti–O in both $(n, 1)$ and $(1, m)$ superlattices, we find that both angles are larger in $(n, 1)$ systems. This suggests that the distortion of octahedrons in the tetragonal lattice of the $(n, 1)$ superlattices is more significant, which results in a larger $\frac{c_0}{a_0}$ ratio displacement.

To investigate the effect of biaxial strain on the structural parameters of unstrained superlattices, the ab plane lattice parameters were varied from −5% to 5%, with a step of 1%. Fig. 3 illustrates the variation of c parameter and volume $versus$ strain for each superlattices. As results, we observe a monotonic decrease in c with increasing strain levels, while the crystal volume increases gradually. At the same time, the average bond lengths d(Sn–O) and d(Ti–O) showed also a reduction under strains, as detailed in Tables S2 and S3 (ESI†). These results suggest that the c axis displays a relatively weak ability to keep the crystal volume constant against biaxial strains, leading to structural and interatomic distances changes. A similar behavior was observed by Wei Zhou and Yanyu Liu when they applied strain on the bc plane of SnO$_2$ bulk.[17]

In Fig. 4, we analysed as well the effect of biaxial strains on the variation of total energy of superlattices using the EOS calculations. Our results show that the superlattices are significantly more susceptible to destabilisation under biaxial

compressive strain ($i.e.$, when $\varepsilon < 0\%$) compared to their response under tensile strain. Furthermore, most superlattices exhibit their most stable energy states in the absence of strain or at very low strain. An exception to this trend is observed in the 3SO/1TO superlattice, which exhibits remarkable resilience to tensile strains, reaching its optimal energy configuration at a strain of 2%, as detailed in Table S4 (ESI†). This unique behaviour highlights the potential for engineering strain to enhance the stability and performance of specific superlattice configurations.

In addition, the total formation energy of the investigated superlattices was computed as described in ref. 33 and 34:

$$E = E_{n\text{SO}/m\text{TO}} - nE_{\text{bulk(SO)}} - mE_{\text{bulk(TO)}} \quad (2)$$

where $E_{n\text{SO}/m\text{TO}}$, $E_{\text{bulk(SO)}}$, and $E_{\text{bulk(TO)}}$ are the total energies of nSO/mTO superlattices, SnO$_2$ and TiO$_2$ bulks, respectively. The results are summarised in Table 2. In particular, the 1SO/3TO structure exhibits the lowest formation energy with 0.0015 eV among the considered systems. The formation energy of $(1, m)$ systems decreases with the increasing number of TiO$_2$ layers. Conversely, the formation energy of $(n, 1)$ systems increases with the increasing number of SnO$_2$ layers. It is also noteworthy that the formation energy of nSO/mTO superlattices increases when the stack contains the same number of oxide layers ($n = m$). These results suggest that as the number of layers of SnO$_2$ and TiO$_2$ is increased simultaneously, the nSO/mTO superlattices become more difficult to form, and the $(n, 1)$ superlattices are relatively more difficult to form than the $(1, m)$ superlattices.

3.2. Dynamical and mechanical stability of the superlattices

To evaluate the dynamic stability of the superlattices, we calculated phonon dispersion curves along with their corresponding total and partial phonon density of states (PhDOS) at equilibrium volumes. Fig. 5 presents the phonon dispersion curves for the 3SO/1TO superlattice which was subjected to a range of biaxial strains (−5%, 0%, and 5%). Detailed phonon spectra and PhDOS for other strain levels on 3SO/1TO superlattice and other compositions are presented in ESI,† Fig. S4–S10. The absence of negative (or imaginary) frequencies, across strain ranging from −5% to 5%, for the 3SO/1TO superlattice
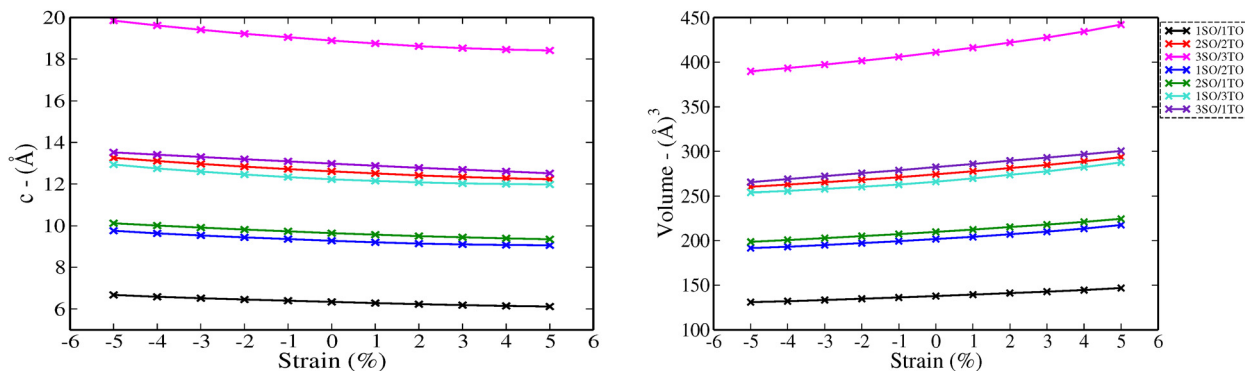

Fig. 3 Structure parameters of nSO/mTO superlattices under biaxial strains from −5% to 5%: c parameters (left) and volumes (right).
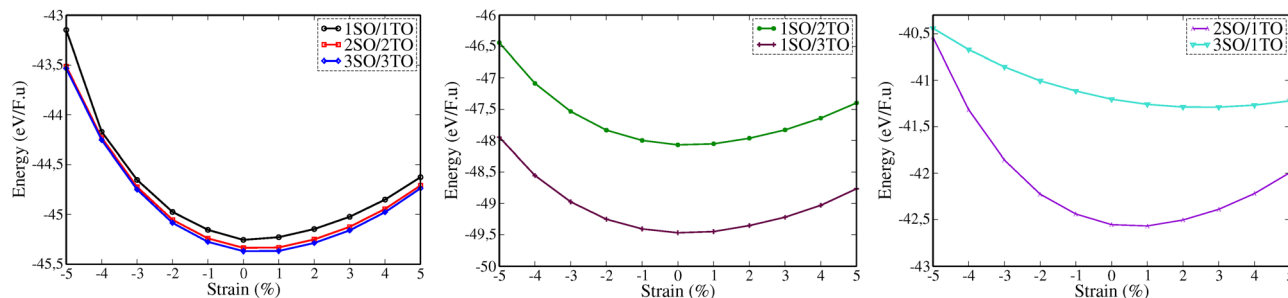
Fig. 4 The total energy–biaxial strain relationship of nSO/mTO superlattices for different stacking periodicity: ($n = m$) left, (1, m) middle, and (n, 1) right.

Table 2 The calculated formation energies for nSO/mTO superlattices

Superlattices	Formation energy (eV)
1SO/1TO	0.2391
2SO/2TO	0.3095
3SO/3TO	0.3763
1SO/2TO	0.1059
1SO/3TO	0.0015
2SO/1TO	0.4264
3SO/1TO	0.6532

confirms its dynamic stability. For the other compositions, the strains at −5%, −4% and 5% involve the presence of imaginary frequencies, indicating a lattice instability. It is noteworthy that strains from −3% to 4% alter the positions of the optical and acoustic phonon bands, yet without extending into the negative frequency domain. Occasional small negative frequencies (<2 THz) at the point arise from numerical artifacts, rather than physical instabilities.

In addition, the PhDOS analysis reveals, for all superlattices, that the vibrational modes at lower frequencies (0 to 8 THz) predominantly originate from the hybridization of Sn and Ti atoms. Conversely, the frequency range from 8 to 25 THz is characterized mainly by the vibrations of O atoms, supplemented by a minor contribution from Ti atoms.

Table 3 presents the highest frequencies observed at the Γ-point in the phonon spectrum for all strained systems. From these data, we observed that tensile strain tends to soften the phonon modes, which can be ascribed to the weakening of atomic bonds (see Tables S2 and S3, ESI†) as the lattice constant increases. Inversely, applying compressive strain involves a shift of phonon modes to higher frequencies, indicative of phonon hardening. It is also noteworthy that both tensile and compressive strains do not influence the contributing states in PhDOS.

Now, considering the tetragonal symmetry of the superlattices, there are six independent elastic constants (C_{11}, C_{33}, C_{44}, C_{66}, C_{12}, and C_{13}) that characterize the mechanical behavior of these structures. Thus, to assess the mechanical stability of the studied superlattices, we evaluated these elastic constants to determine if they fulfill the Born–Huang stability criteria.[35] For this investigation, the unstrained nSO/mTO superlattices served as model systems, and their elastic

constants were meticulously calculated. Using the Voigt-Reuss-Hill (VRH) approximation,[36,37] we derived the macroscopic mechanical properties including the bulk modulus (B), the shear modulus (G), the Young's modulus (E), the Poisson's ratio (n), and the Debye temperature ($\theta_{\rm D}$). The calculated elastic constants are presented in Table S5 (ESI†) and their corresponding mechanical properties are detailed in Table S6 (ESI†). For all examined superlattices, the calculated elastic constants C_{ij} (expressed in GPa) are positive and comply with Born's stability criteria, confirming that the unstrained nSO/mTO superlattices will not mechanically fail when subjected to expected loads and stresses. Moreover, It was observed that the stacking periodicity exerts a more significant influence on the shear elastic constant C_{44} than on the other elastic constants C_{ij}. This finding underlines the critical role of structural configuration in determining the mechanical properties of these materials.

The bulk modulus (B) quantifies the degree of change in resistance with respect to volume change and indicates its hardness. Our calculations revealed that superlattices containing one (SnO$_2$) layer and three (TiO$_2$) layers (1SO/3TO) possess the highest bulk modulus. In contrast, the inverse configuration (3SO/1TO) exhibits the lowest bulk modulus. The shear modulus (G) is a measure of a materials response to shear stress, reflecting the deformation that occurs when a parallel force is applied to one surface while an opposing surface resists. From the present study, the superlattice comprising one layer of SnO$_2$ and two layers of TiO$_2$ (1SO/2TO) exhibited the greatest shear modulus.

Furthermore, the ductility of nSO/mTO superlattices was assessed using the Pugh criterion and Poisson's ratio (ν) as indicators.[38] According to Pugh's criterion, materials with a ratio of bulk modulus (B) to shear modulus (G) greater than 1.75 are likely to manifest ductile behavior, while those with a $\frac{B}{G}$ ratio less than 1.75 are expected to be brittle. Similarly, materials with a Poisson's ratio greater than 0.26 are generally considered as ductile, whereas those with ν less than 0.26 are typically classified as brittle.[39,40] Our calculations revealed a $\frac{B}{G}$ ratio greater than 1.75 for superlattices containing more than one TiO$_2$ layer, indicating ductile behavior according to the Pugh criterion (see Fig. 6). Correspondingly, the Poisson's ratio

1288 | *Phys. Chem. Chem. Phys.*, 2025, **27**, 1284–1297
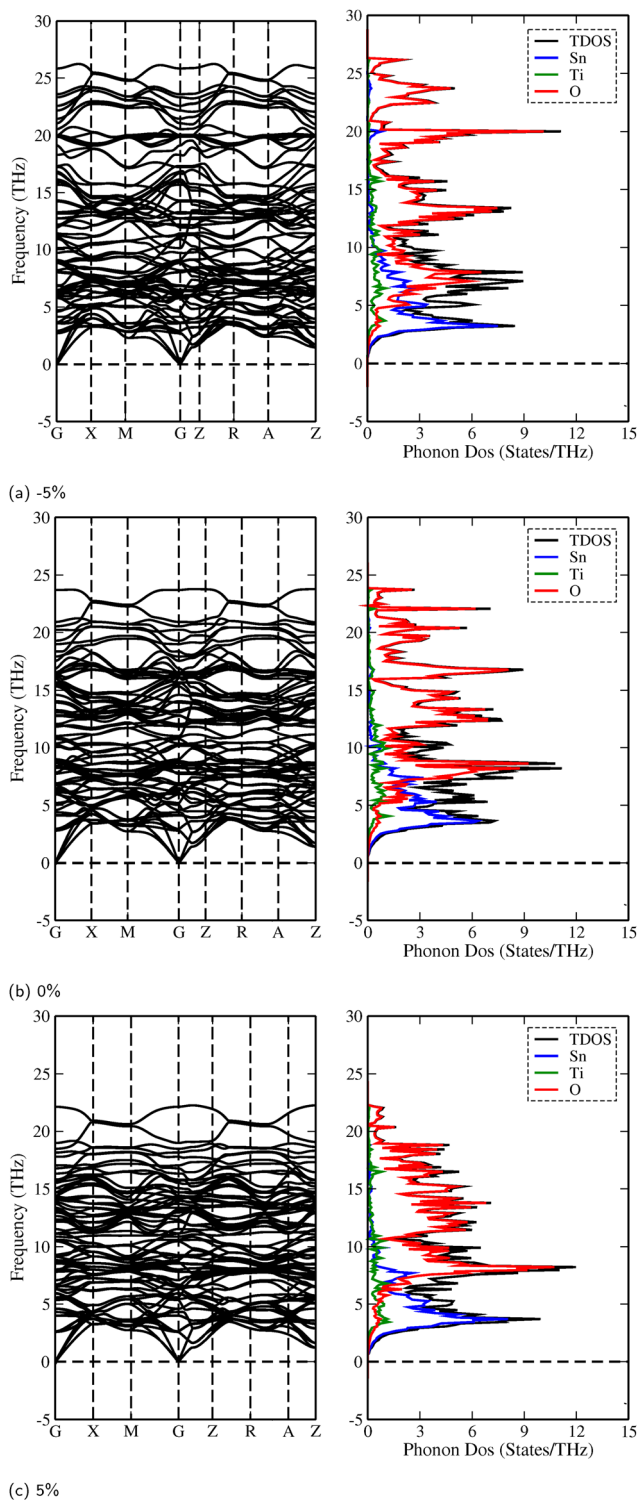
This journal is © the Owner Societies 2025

Fig. 5 (a)–(c) Phonon dispersion curves and phonon densities of states of unstrained (middle) and strained 3SO/1TO superlattices under biaxial compressive (upper part) and tensile (bottom part) strain.

Table 3 Upper limit of optical branches for the nSO/mTO superlattices at lower and upper limits of dynamically stable biaxial strains

Superlattices	Strain limits (%)	Freq. (THz)
1SO/1TO	−3	25.55
	4	22.27
2SO/2TO	−3	26.15
	4	22.45
3SO/3TO	−3	26.22
	4	23.43
1SO/2TO	−3	26.16
	4	23.12
1SO/3TO	−3	26.27
	4	22.36
2SO/1TO	−3	25.79
	4	22.32
3SO/1TO	−5	25.71
	5	22.09

characteristics of the material. In fact, Poisson's ratio provides insights into the nature of atomic bonding. Ionic crystals typically exhibit Poisson's ratios between 0.25 and 0.33, while covalent materials range from 0.10 to 0.25. Our calculated Poisson's ratios, ranging from 0.25 to 0.28, suggest a mixed iono-covalent bonding character. The 1SO/3TO superlattice, which has the highest bulk modulus and $\frac{B}{G}$ ratio values, displays a more ionic bonding character than the 3SO/1TO superlattice, which has a more covalent bonding character. The covalent character allows for greater atomic rearrangement and plastic deformation under applied strain, explaining the stability of the 3SO/1TO superlattice under strain ranging from −5% to 5%.

Young's modulus (E) is the ratio between stress and strain, providing a measure of the stiffness of the material. It can be seen from Fig. 6 that 1SO/2TO is the stiffest superlattice, exhibiting the highest value of E. It is also observed that in both $(n, 1)$ and $(n = m)$ configurations, Young's modulus decreases with increased stacking, indicating a reduction in stiffness for these superlattices.

The Debye temperature (θ_D) can be used as a proxy to quantify structural rigidity. Indeed, a higher θ_D indicates stronger interatomic bonding and greater structural rigidity, while a lower θ_D suggests weaker bonding and more anharmonicity in the lattice vibrations.[41] By comparing θ_D of the studied superlattices, we found that the bonding strength in the $(1, m)$ and $(n = m)$ stacking structures is stronger. This suggests that the weaker interatomic bonding contributes to the brittleness in the $(n, 1)$ stacking structures. The 3SO/1TO superlattice presents the lowest θ_D value and hence a low structural rigidity, confirming our previous findings.

Strain–stress curves under biaxial strain from −5% to 5% are shown in Fig. 7. As expected, the stress increases 'linearly' from 1 to 5%. Similarly, for compressive strains from −1% to −5%, the stress increases 'linearly' up to a maximum value at −5%. Furthermore, we observed that the resulting stress depends on the composition of the superlattices, particularly on the number of SO layers. The greater the number of SO layers, the higher the stress generated for the same applied
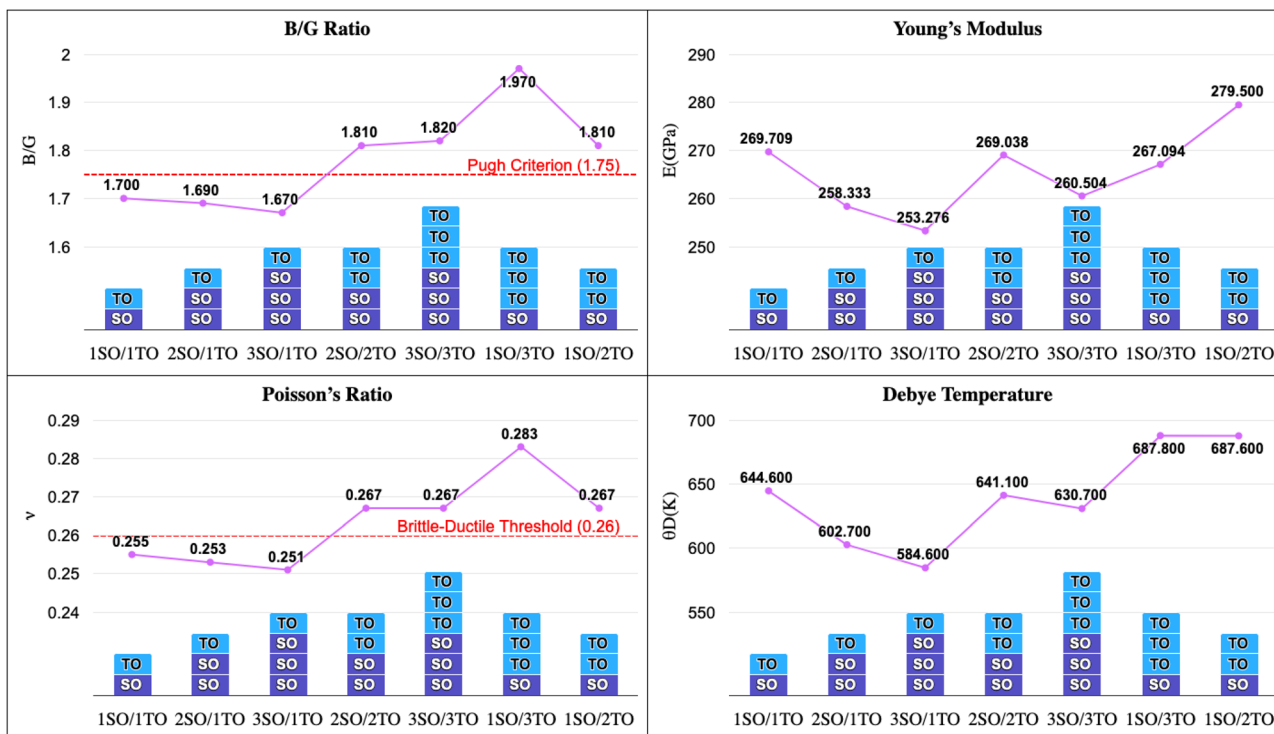
for those superlattices was found to be greater than 0.26, further supporting the prediction of ductile behavior. The agreement between the Pugh criterion and Poisson's ratio can be attributed to the underlying atomic bonding and structural

Fig. 6 Evolution of $\frac{B}{G}$ ratio, Young's modulus (E), Poisson's ratio (n), and Debye temperature (θ_D) of unstrained nSO/mTO superlattices for different (n/m) stacking periodicities.
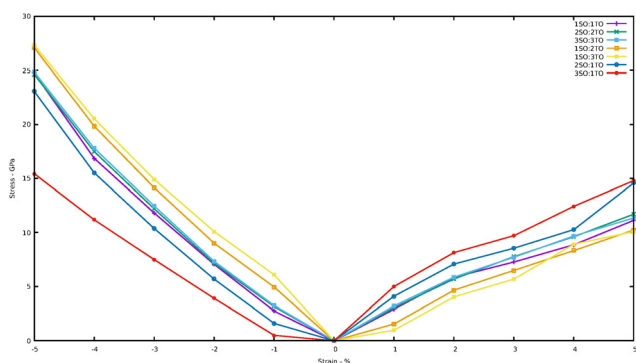

Fig. 7 Strain–stress curves of nSO/mTO superlattices.

strain. This behavior can be directly related to the mechanical properties calculated at 0% (Fig. 6). The decrease in E for nSO/1TO superlattices indicates that these materials are more flexible and deform more easily under strain, leading to higher stress values for nSO/1TO compared to 1SO/nTO. Additionally, the observed decrease in the $\frac{B}{G}$, (ν) and (θ_D) supports this behavior, as the material's tendency to become more brittle with increasing SO layers contributes to the generation of higher stresses when the biaxial strain increases to 5%. While high stresses may limit certain practical applications, these results are particularly interesting for theoretical and applied studies aiming to exploit strain-induced electronic effects in these materials.

3.3. Electronic properties of the superlattices

To better understand the impact of stacking configurations (n/m) on the electronic properties of dynamically stable nSO/mTO superlattices, we conducted a comprehensive analysis of their energy band structures and electron density of states (DOS). To do so, We employed the HSE06 functional, renowned for its precision in predicting electronic band structures. In particular, the calculated band gaps for both SnO_2 and TiO_2 bulks were found to be 3.42 eV and 3.35 eV, respectively. These values closely align with the experimental band gaps of 3.60 eV for SnO_2[42] and 3.10–3.30 eV for TiO_2.[43,44] It is worth noting that a direct fundamental gap at the Γ-point was confirmed for both materials. The slight deviations observed between our computational results and the experimental data are probably attributed to the inherent limitations of DFT.

The band gaps of the unstrained superlattices, as well as bulk SnO_2 and TiO_2, calculated using PBE, GGA+U, and HSE06 functionals, are presented in Table 4. The three functionals consistently predict similar trends in the variation of band gaps, which exhibit a slight decrease with increasing stacking periodicity. Importantly, the calculated band gap values remained relatively close to those of the parent materials, specifically SnO_2 and TiO_2, indicating that the stacking periodicity (n/m) has a minimal impact on both the nature and magnitude of the band gap, which continue to lie outside the visible light spectrum. Fig. 8 displays the band structures calculated using the HSE06 functional, which indicate that all superlattices maintain the direct band gap characteristic at the Γ-point.

1290 | *Phys. Chem. Chem. Phys.*, 2025, **27**, 1284–1297

This journal is © the Owner Societies 2025

Table 4 Stacking effect on the band gaps (eV) calculated with GGA-PBE, GGA+U, and HSE06 approximations for the unstrained nSO/mTO superlattices. These values are compared to SnO$_2$ and TiO$_2$ bulk reference values

System	GGA-PBE (eV)	GGA+U (eV)	HSE06 (eV)	Exp. (eV)
SO	1.121	1.204	3.423	3.600[42]
TO	1.834	3.211	3.353	3.100–3.300[43,44]
1SO/1TO	1.820	2.850	3.455	
2SO/2TO	1.765	2.142	3.438	
3SO/3TO	1.668	1.912	3.253	
1SO/2TO	1.817	2.363	3.448	
1SO/3TO	1.807	2.307	3.335	
2SO/1TO	1.849	2.903	3.532	
3SO/1TO	1.545	1.712	3.208	

The total and partial DOS (Fig. 9) for both SnO$_2$ and TiO$_2$, as well as for the unstrained nSO/mTO superlattices, indicate that the top of the valence band (VB) in all structures predominantly consists of O(2p) states. In contrast, the conduction band (CB) is primarily composed of Sn(5s), Sn(5p) and/or Ti(3d) states. The presence of O(2p), Sn(5s), Sn(5p), and Ti(3d) states in both the VB and CB suggests a significant degree of hybridization in the metal–oxygen bonds.

To elucidate the relationship between lattice strain and electronic properties of dynamically stable nSO/mTO superlattices, we have calculated band structures, total and partial DOS under biaxial strain, as shown in Fig. S12–S17 (ESI†). The results confirm that the direct bandgap character is preserved for all superlattices under both tensile and compressive strains. Furthermore, analysis of the PDOS curves shows that, neither tensile nor compressive strains affect the nature of the contributing states into valence and conduction bands. Fig. 10 shows the band gap variations under these conditions. The energy levels of the CB minima and VB maxima for these superlattices are summarised in the ESI† (Tables S7–S9). When we examined the band gap evolution of all the studied superlattices, we found that they are significantly affected by biaxial tensile strain, which reduces the band gap values. The 2SO/1TO superlattice exhibited the smallest band gap of 2.33 eV at 4% tensile strain. A comparison of the band structures (Fig. 11) under 0% and 4% tensile strain for this structure shows that while the highest valence subband undergoes minimal change and moves closer to the Fermi level, the lowest conduction subband undergoes more pronounced changes resulting in reduced band gaps. In contrast to the tensile case, compressive strains resulted in a smaller decrease or even an increase in the band gap of the 3SO/1TO superlattice. This finding can be explained by the variation of metal–oxygen bond lengths. Indeed, for all superlattices, except the 3SO/1TO one which has the lowest $\frac{B}{G}$ ratio, the 'd(Sn, Ti)–O' distance along the (110)
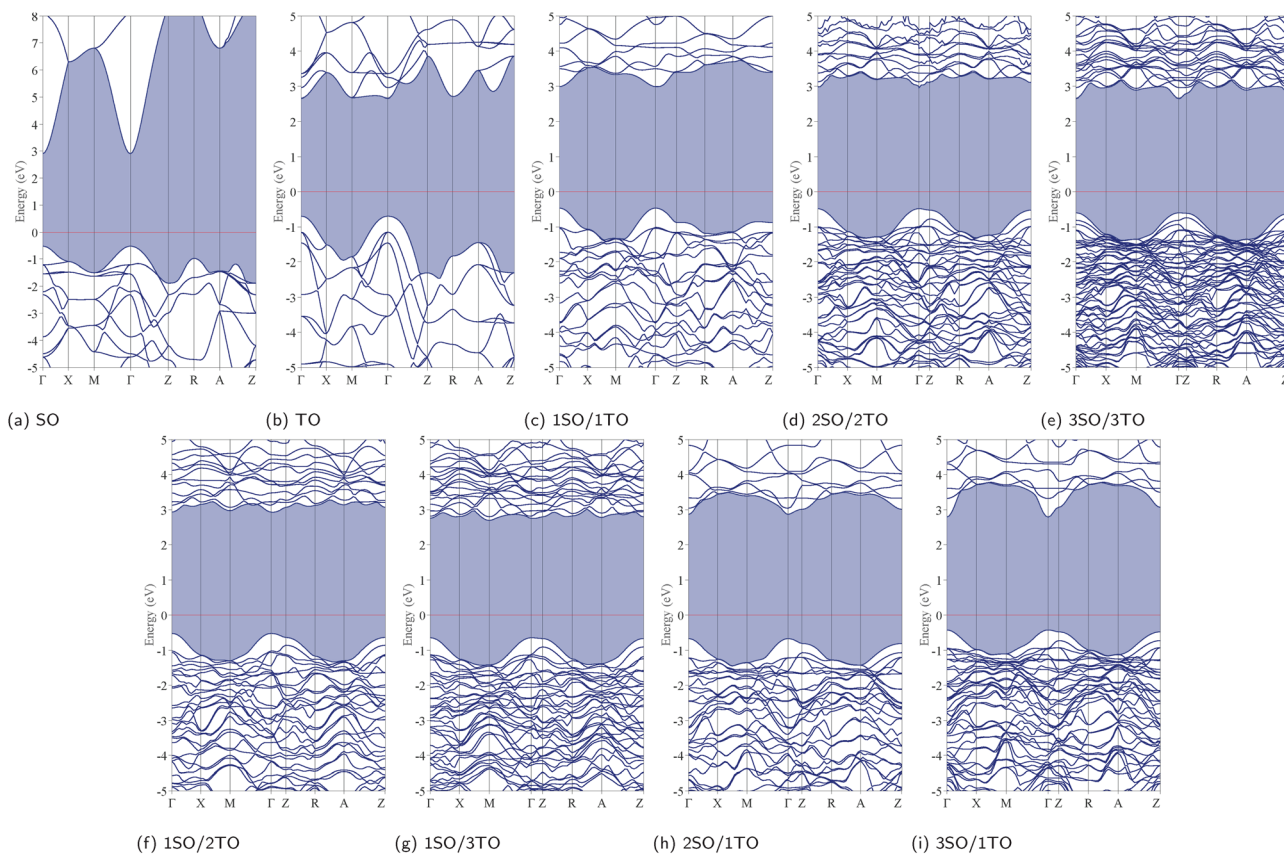

Fig. 8 (a)–(i) Band structures of SnO$_2$ and TiO$_2$ bulks compared to unstrained nSO/mTO superlattices. These electronic structures have been obtained at DFT-HSE06 level of theory. The Fermi level is located at zero electron-volt (the blue shaded areas correspond to energies between the highest valence bands and the lowest conduction bands).
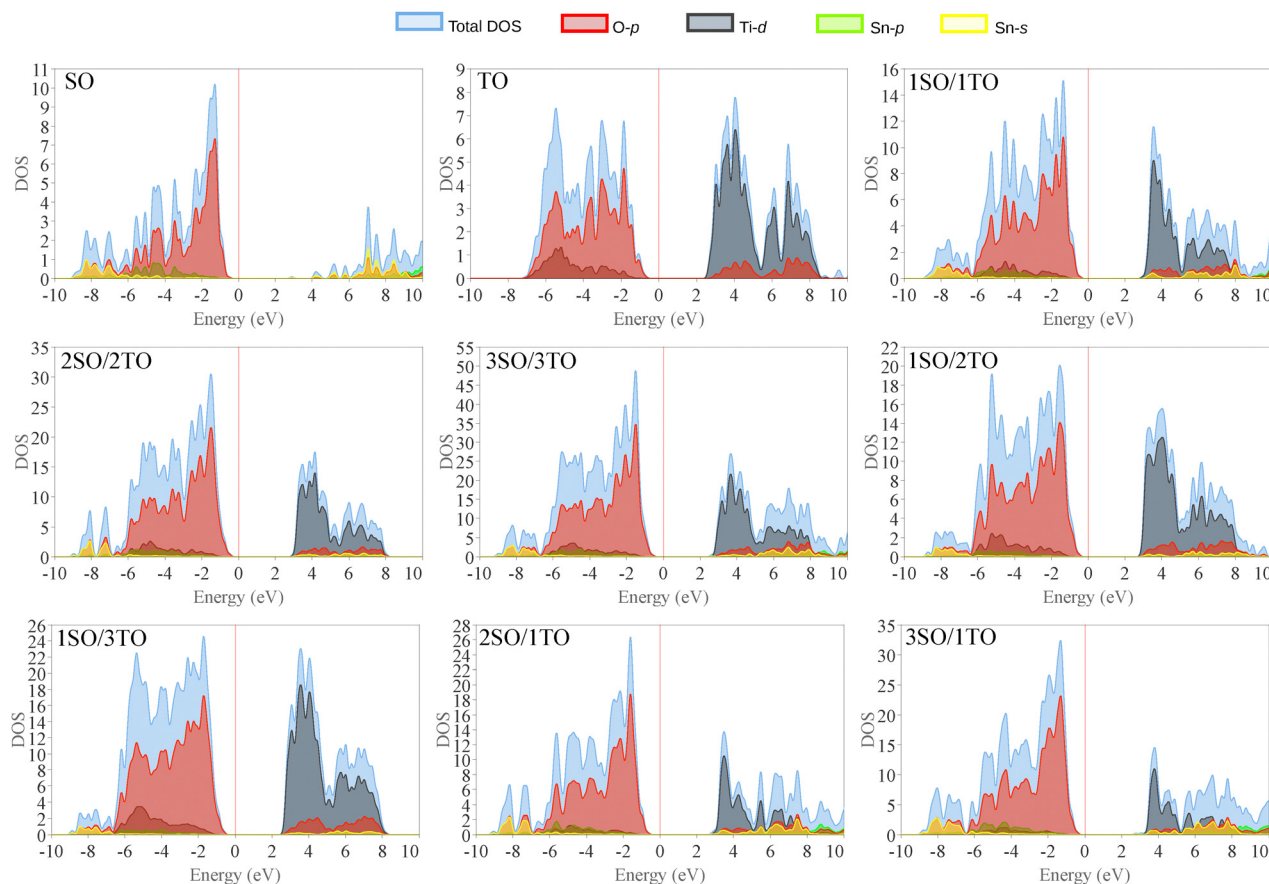
Fig. 9 Density of states (DOS) of SnO_2 and TiO_2 bulks compared to unstrained nSO/mTO superlattices. These DOS have been obtained at DFT-HSE06 level of theory. The Fermi level is located at zero electron-volt.

plane (Fig. S11, ESI†) remains constant with increasing compressive strain. In the case of the 3SO/1TO superlattice, the band gap increases linearly with increasing compressive strain. A similar behavior is observed for the bulk SnO_2 and TiO_2 systems.

Analysis of the contributions of the Ti-d, Sn-s and O-p orbitals to the DOS of 3SO/1TO (Fig. 12) and other superlattices (Fig. S18–S23, ESI†) showed that the energies of these orbitals in the VB states remain unaffected under both compressive and tensile strains. However, in the CB, under compressive strain these orbitals shift towards the Fermi level for all superlattices, except the 3SO/1TO composition. In this last superlattice, the Ti-d, Sn-s and O-p orbitals move away from the Fermi level, explaining the observed increase in the band gap value shown in Fig. 10. Furthermore, near to VB maxima, the peaks of intensity of partial DOS for the O-$2p_x$, O-$2p_y$, and O-$2p_z$ orbitals exhibit different variation trends. It suggests a distortion in the XO_6 (X = Sn, Ti) octahedron structures, that is consistent with our crystal structure analysis.

3.4. Electron localization function of superlattices

To gain further insight into the effect of biaxial tensile and compressive strain on the character of the bond, we calculated the electron localization function (ELF) of nSO/mTO

superlattices projected on the (110) plane, as plotted in Fig. 13 for 3SO/3TO structure. ELF is a powerful tool that can be used to determine the spatial localization of electrons in crystals.[45] It takes values between 0 and 1, showing the type and strength of the bond. A low ELF value indicates a deficit of shared electrons between two atoms, representing an ionic bond. Conversely, a high ELF value signifies abundant electron sharing between two atoms, characteristic of a covalent bond with various bonding strength.

It is found that the chemical bonding in nSO/mTO superlattices is predominantly characterized by ionic Sn–O and Ti–O bonds, with a minor covalent component. This covalent character is less pronounced between Ti and O atoms, as indicated by the calculated Poisson's ratios (see Section 3.2). In addition, this covalent character slightly increases under biaxial compressive strain and decreases with increasing tensile strain.

3.5. Effective mass of electrons and holes in the superlattices

The assessment of semiconductor materials for photocatalytic water splitting applications strongly relies on the mobility of photo-excited pair of charges. A theoretical evaluation of this mobility can be drive from the effective mass of created excitons (electrons/holes). In fact, it was proved that the drift velocity of charge carriers is inversely proportional to the
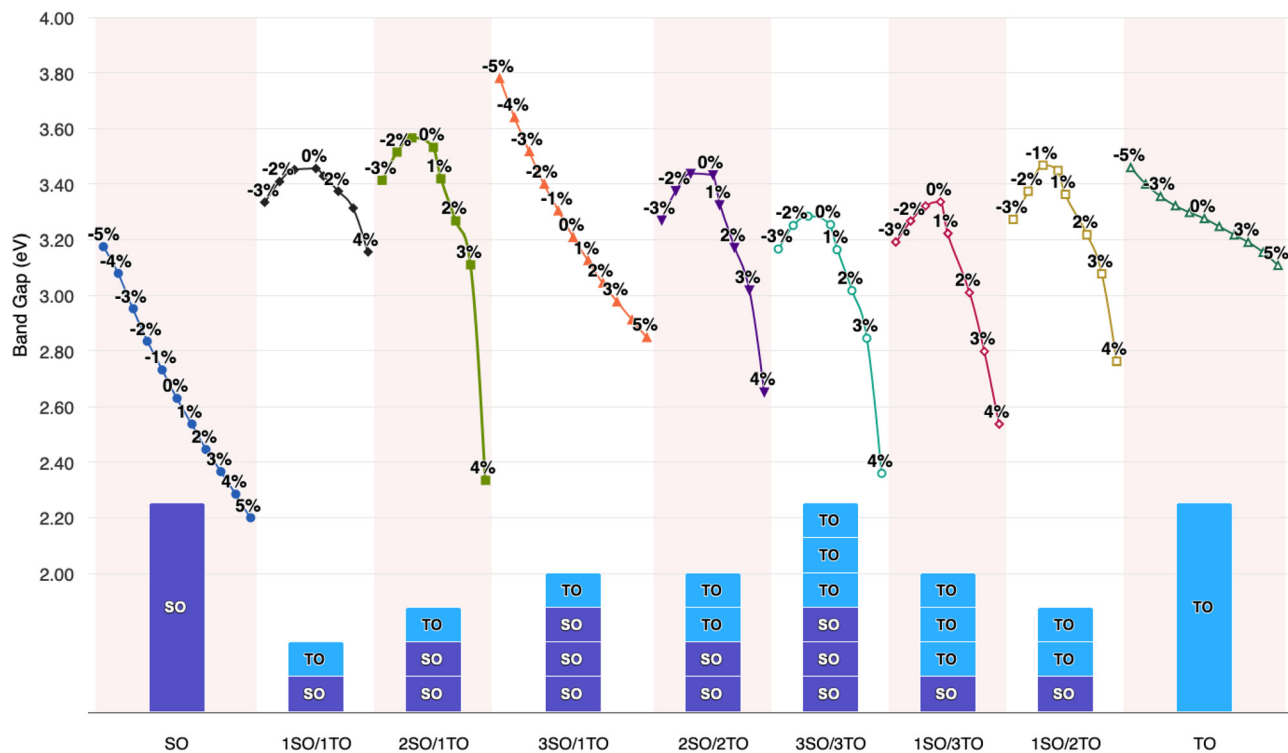
1292 | *Phys. Chem. Chem. Phys.*, 2025, **27**, 1284–1297

This journal is © the Owner Societies 2025

Fig. 10 Biaxial strain effect on the band gap of XO_2 (X = Sn, Ti) metal oxides and nSO/mTO superlattices.
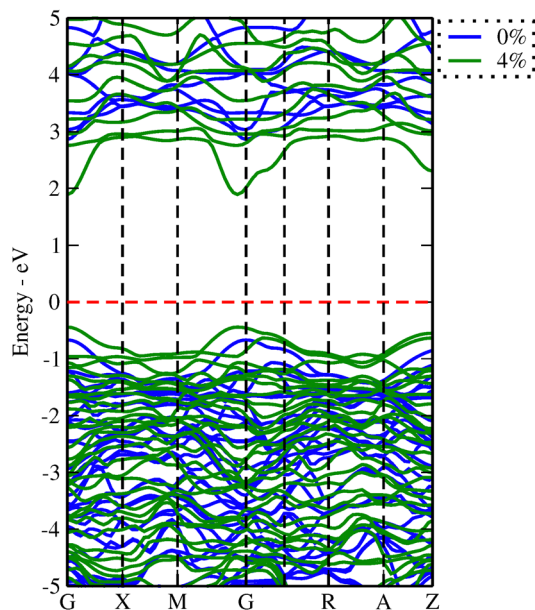

Fig. 11 Band structures for the 2SO/1TO under 0% (blue) and 4% (green) tensile strain. The Fermi level is located at 0 electron-volt.

effective mass, as defined in the equation below:[46]

$$v = \frac{\hbar k}{m^*} \qquad (3)$$

where v, k, $\hbar$, and m^* represent the velocity of photogenerated charge carriers, the wave vector, the reduced Planck constant, and the effective masses of electrons and holes, respectively.

The high mobility of photo-excited pair of charges is observed when they have small effective mass. This reduces the chance of recombination between the electrons and holes. The charge carriers can easier reach the material surface where occurs the reaction. To obtain the effective masses of particles in the different hetero-junctions, we fitted in the Brillouin zone their VB and CB extrema by a parabolic function and we applied before the following equation:

$$m^* = \pm\hbar^2 \left(\frac{\mathrm{d}^2 E}{\mathrm{d}k^2}\right)^{-1} \qquad (4)$$

where E represent the energy of an electron at wavevector k in that band. The positive sign corresponds to the effective mass of electrons, while the negative sign corresponds to the effective mass of holes.

In the Table 5 we present the calculated effective electron and hole masses of bulk SnO_2, TiO_2 and nSO/mTO superlattices under various strain conditions. The values are obtained by averaging the second derivative in both the Γ to Z and Γ to M directions, providing a more accurate estimate of the effective masses. Available experimental values for the bulk oxides are also included for comparison.[47,48] Our calculated effective electron masses are in good agreement with the experimental results, with a larger mass in TiO_2 than in SnO_2. To our knowledge, no experimental data have been reported for the effective hole masses in either oxide. However, our calculated

This journal is © the Owner Societies 2025

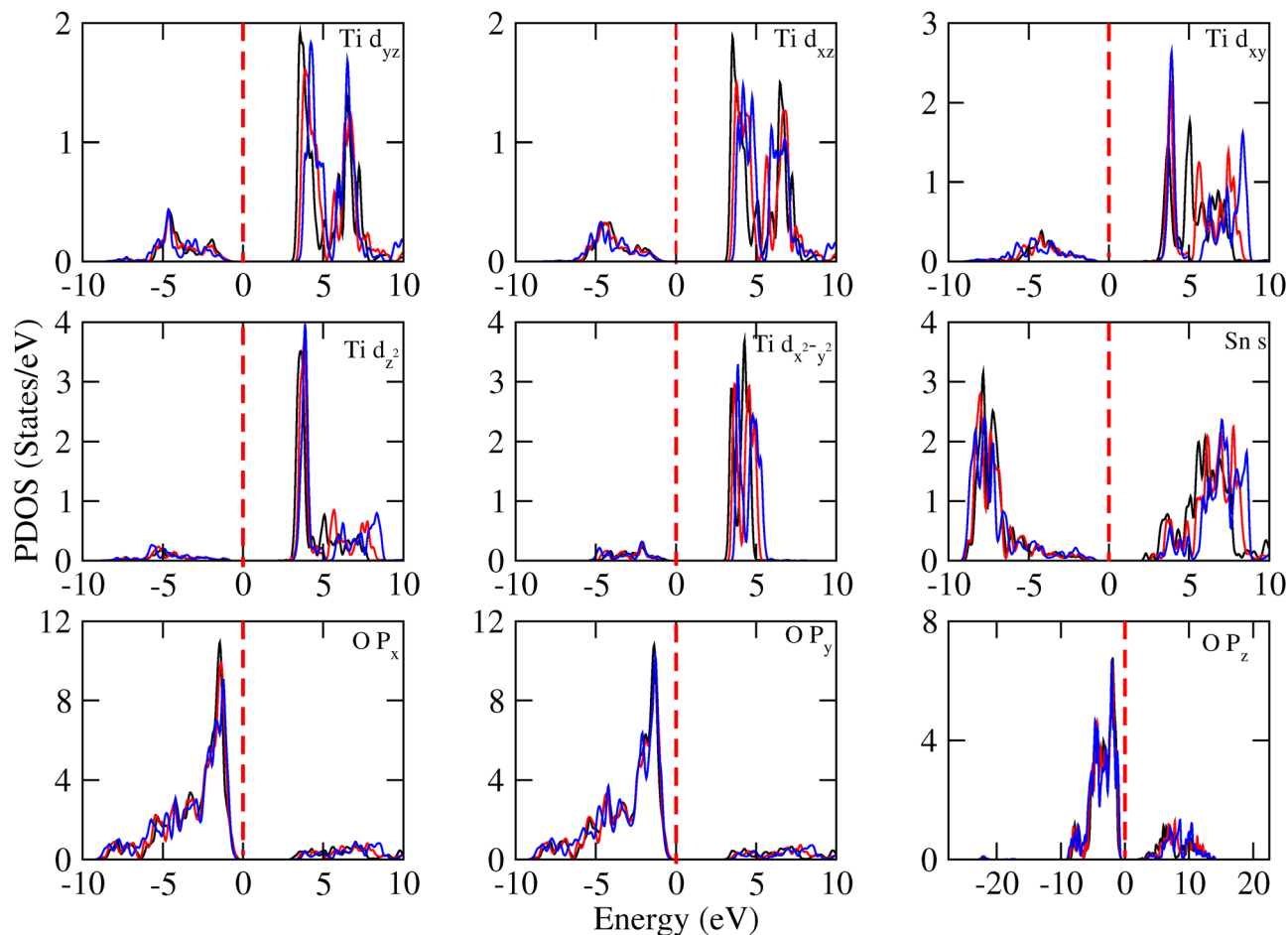*Phys. Chem. Chem. Phys.*, 2025, **27**, 1284–1297 | **1293**

Fig. 12 Contributions into DOS of Ti-d, Sn-s and O-p orbitals for the 3SO/1TO superlattice under upper limits −5% (black), 0% (red) and 5% (blue) biaxial strains.

values show large effective hole masses in good agreement with previous theoretical results.[46,49,50]

The (n/m) stacking periodicity in superlattices has been shown to affect the effective masses of charge carriers; there is a significant decrease in the effective masses of electrons compared to those of holes, with the latter showing a slight increase in effective mass with increasing layers. To illustrate, the effective mass of electrons in the unstrained 3SO/3TO superlattice is 0.573 m_0, which is eight times smaller than that observed in the 1SO/1TO superlattice. The application of biaxial tensile strain leads to a decrease in the effective mass of electrons and an increase in the effective mass of holes. Conversely, the opposite trend is observed under compressive biaxial strain. It is expected that superlattices with 1SO/3TO and 3SO/1TO periodicity under 4% and 5% tensile strain, respectively, will enhance the mobility of photogenerated carriers compared to the single SnO$_2$ and TiO$_2$ parent phases.

To qualitatively assess the charge separation rate, we used the relative ratio $D = \mathrm{abs}\left(\dfrac{m_h^*}{m_e^*}\right)$. A high value of this ratio indicates a greater tendency into material to separate charges, implying a lower recombination rates that enhances the photocatalytic activity.[51] For all superlattices, the effective mass ratio

D decreases under compressive strain and increases under tensile strain, suggesting that the transfer rate of holes and electrons is faster under tensile strain than under compressive strain. This leads to higher photocatalytic activity under tensile strain compared to compressive strain.

3.6. Photocatalytic properties of the superlattices

Reducing the band gaps is not enough to improve the photocatalytic activity of nSO/mTO superlattices. The band edges also need to be better aligned with the water potentials. For efficient photocatalytic water splitting, it is necessary that the top of the VB energy must be more positive than the oxidation potential of O$_2$/H$_2$O (1.23 eV). Inversely, the bottom of the CB energy must be more negative than the reduction potential of H$^+$/H$_2$ (0 eV).

The alignment of the position of band edges can be achieved by the electronegativity[52] of each atom composing the structure, using these equations:

$$E_{\mathrm{VBM}}^{\mathrm{pH}=0} = \chi - E_0 + \frac{1}{2}E_{\mathrm{g}}, \qquad (5)$$

$$E_{\mathrm{CBM}}^{\mathrm{pH}=0} = E_{\mathrm{VBM}}^{\mathrm{pH}=0} - E_{\mathrm{g}}. \qquad (6)$$

1294 | *Phys. Chem. Chem. Phys.*, 2025, **27**, 1284–1297
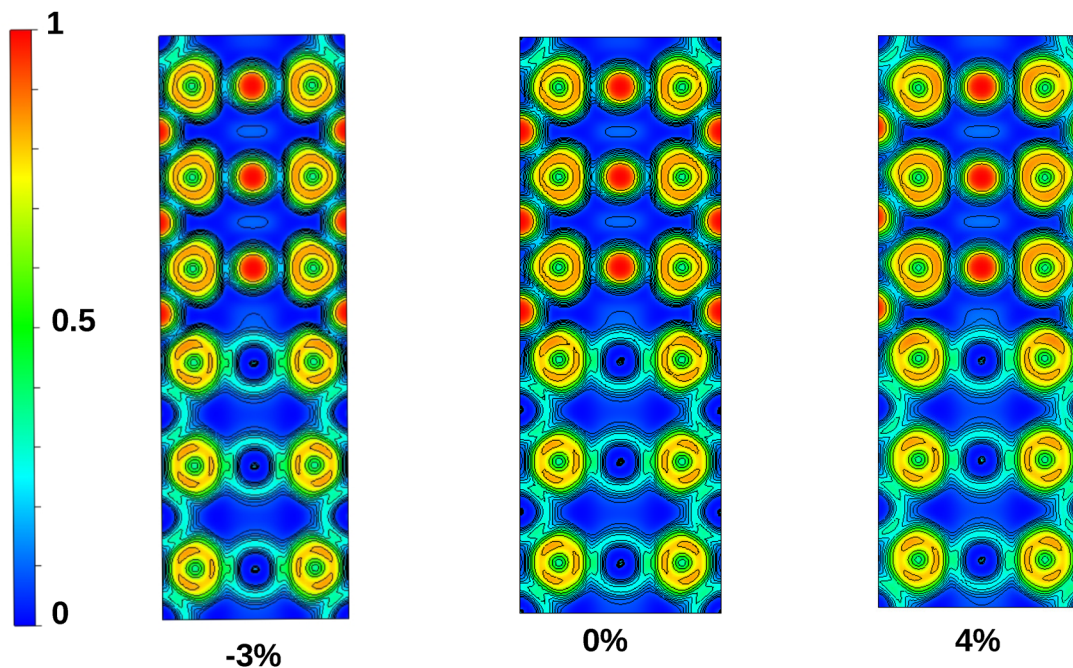
This journal is © the Owner Societies 2025

Fig. 13 Electron localization function (ELF) graphs of projected 3SO/3TO superlattice on the (110) plane.

Table 5 The calculated effective mass of holes and electrons in m_0, and the relative effective mass ratio of bulk (XO_2, X = Sn, Ti), and nSO/mTO superlattices under strain limits

	Strain (%)	m_h^*	$m_{e^-}^*$	D
SO		−1.306	0.273	4.783
			0.287[47]	
TO		−1.826	1.215	1.502
			2.000[48]	
1SO/1TO	−3	−1.377	7.367	0.186
	0	−1.449	5.013	0.289
	4	−1.565	1.543	1.014
2SO/2TO	−3	−1.366	1.074	1.271
	0	−1.545	1.033	1.495
	4	−1.908	0.931	2.049
3SO/3TO	−3	−1.375	0.868	1.584
	0	−1.646	0.573	2.872
	4	−1.751	0.502	3.488
1SO/2TO	−3	−1.373	1.664	0.825
	0	−1.548	3.659	0.423
	4	−2.003	1.468	1.364
1SO/3TO	−3	−1.440	1.626	0.885
	0	−1.750	1.249	1.401
	4	−2.014	0.305	6.603
2SO/1TO	−3	−1.347	1.036	1.300
	0	−1.454	0.539	2.697
	4	−1.541	0.413	3.731
3SO/1TO	−5	−1.486	0.436	3.408
	0	−1.529	0.377	4.055
	5	−1.528	0.305	5.009

These alignments can be as well adjusted with the specific pH using this last equation:

$$E_{CBM,VBM}^{pH} = E_{CBM,VBM}^{pH=0} - 0.05911 \times pH. \tag{7}$$

where, E_{VBM} and E_{CBM} are the VBM and CBM potentials of the nSO/mTO superlattices. χ refers to the absolute electronegativity. Values of 4.30, 3.45, and 7.54 have been used for χ_{Sn}, χ_{Ti}, and χ_O, respectively. $E_0 = 4.5$ eV is the energy of free electrons on the hydrogen scale.

The band edge alignment at pH equal 0, 7 and 14 was calculated under the biaxial applied strain by rescaling the above equations according to the nSO/mTO superlattices (see the equations in ESI†). Here, only the VBM and CBM positions of 2SO/2TO, 3SO/3TO, 1SO/2TO, 1SO/3TO and 2SO/1TO which have band gaps less than or equal to 2.7 eV, have been displayed. The band-edge alignments for 1SO/3TO and 3SO/3TO superlattices when pH equal 0, 7 and 14 are plotted in Fig. 14, while remaining results are summarized in Fig. S24–S26 (ESI†).

For all superlattices at pH = 0, the VBM edges are consistently higher than the standard oxidation potential of O_2/H_2O and decrease under biaxial strain. Conversely, the CBM edges are slightly higher than the redox potentials of H^+/H_2 and even fall below this potential under biaxial strain, which is not desirable for catalytic applications. The band edges can be tuned by increasing the pH to 7 or 14, as show in Fig. 14. Indeed, for the mechanically stable 1SO/3TO and 3SO/3TO superlattices, which exhibit an optimal band gap value at 4% biaxial tensile strain, the VBM and CBM edges are well aligned with the water redox potentials, making them promising for photocatalytic applications.

4. Conclusions

In this study, we have systematically investigated the effects of biaxial strain on the structural, electronic, and photocatalytic properties of $(SnO_2)_{(n)}/(TiO_2)_{(m)}$ superlattices using DFT

This journal is © the Owner Societies 2025

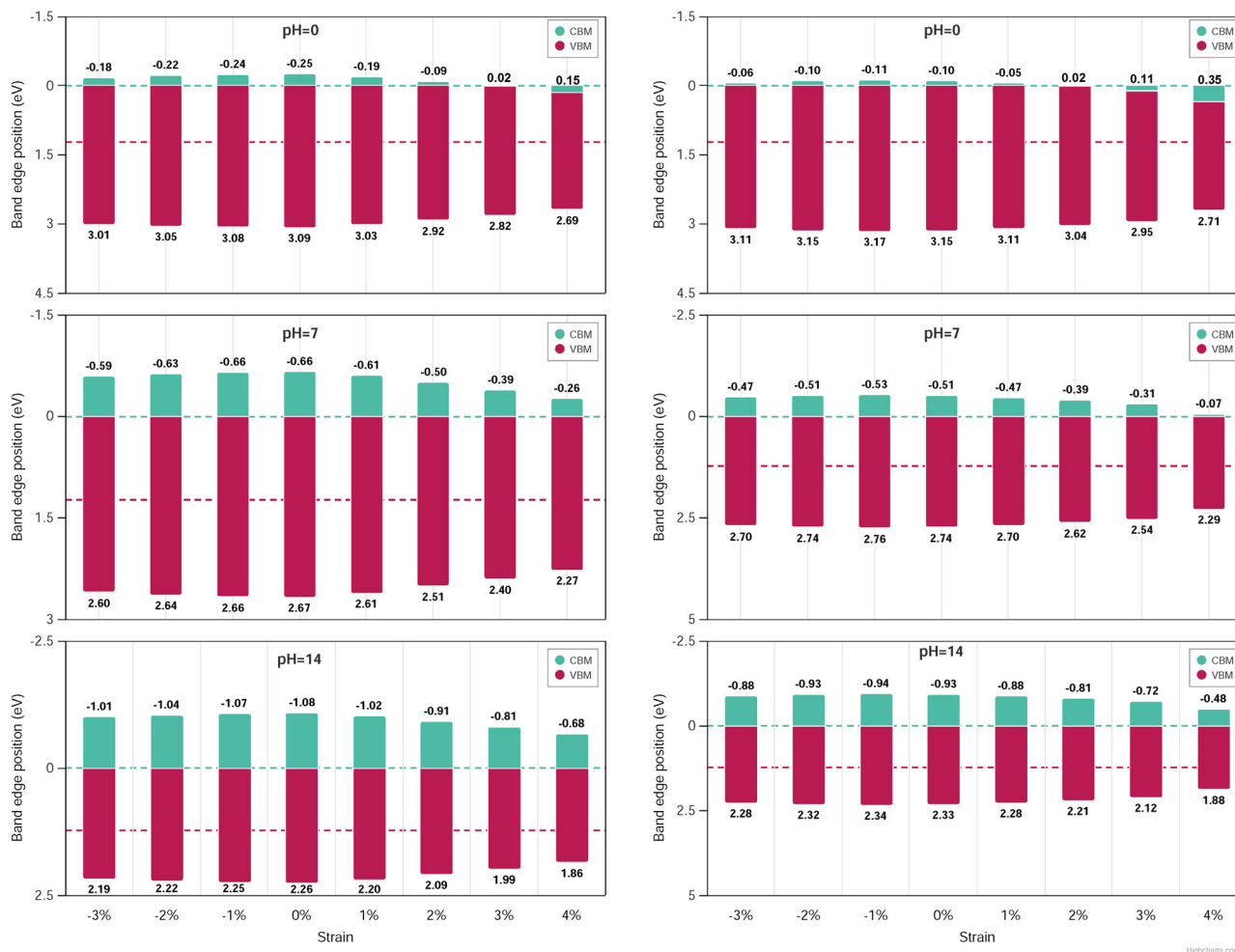*Phys. Chem. Chem. Phys.*, 2025, **27**, 1284–1297 | **1295**

Fig. 14 Band edges alignment for 1SO/3TO (left) and 3SO/3TO (right) superlattices under biaxial tensile and compressive strains when pH equal 0 (upper part), 7 (middle part) and 14 (bottom part). The horizontal dashed lines are the water redox potentials.

calculations. Our findings demonstrate that these superlattices exhibit excellent mechanical stability according to the Born's criteria and reveal that stacking periodicity $(1, m)$ presents the highest bulk modulus, Poisson's ratio and Debye temperature values. Phonon dispersion analysis shows that the 3SO/1TO superlattice maintains dynamic stability under both tensile and compressive strains ranging from -5% to 5%, while other superlattices remain stable within the range of -3% to 4%. For all the considered superlattices, the band gap is effectively tuned by tensile strain. For instance, the tunability of the band gap with strain is particularly noteworthy, with a range from 3.34 eV to 2.54 eV under tensile strains for the 1SO/3TO super-lattice, which also exhibits high carrier mobility. Our analysis further highlights the potential of these superlattices as efficient photocatalysts for water splitting, as indicated by favorable band edge alignments at different pH levels.

In summary, the incorporation of strain engineering in $(SnO_2)_{(n)}/(TiO_2)_{(m)}$ superlattices offers a promising avenue for optimizing their properties for photocatalytic applications, specifically in the realm of hydrogen production from water splitting.

Author contributions

NH and AS conceived the study, carried out the modeling, calculations and analyzed the data, writing the first drift. AS and BC contributed on editing and reviewing the manuscript.

Data availability

Data for this article have been included as part of the ESI† and are available at **https://doi.org/10.5281/zenodo.13350149**.

Conflicts of interest

There are no conflicts to declare.

Acknowledgements

Notes and references

1 Q. Xiang, B. Cheng and J. Yu, *Angew. Chem., Int. Ed.*, 2015, **54**, 11350–11366.

2 J. Han, J. Guo, H. Liu, Y. Han, J. Wang, X. Ma, B. Yan, B. He and W. Lu, *J. Phys. Chem. C*, 2024, **128**(3), 1116–1121.

3 G. R. Portugal, R. M. Ronchi, S. F. Santos and J. T. Arantes, *Surf. Interfaces*, 2023, **36**, 102486.

4 M. Ashwin Kishore, K. Larsson and P. Ravindran, *ACS Omega*, 2020, **5**, 23762–23768.

5 G. Wang, J. Chang, W. Tang, W. Xie and Y. S. Ang, *J. Phys. D: Appl. Phys.*, 2022, **55**, 293002.

6 D. Voiry, H. S. Shin, K. P. Loh and M. Chhowalla, *Nat. Rev. Chem.*, 2018, **2**, 0105.

7 N. Hassan, A. Jalil, N. Khusnun, A. Ahmad, T. Abdullah, R. Kasmani, N. Norazahar, M. Kamaroddin and D. Vo, *Environ. Chem. Lett.*, 2022, 1–23.

8 F. Mikaeili, T. Gilmore and P.-I. Gouma, *Catalysts*, 2022, **12**, 1303.

9 A. Fujishima and K. Honda, *Nature*, 1972, **238**, 37–38.

10 A. Janotti, J. Varley, P. Rinke, N. Umezawa, G. Kresse and C. Van de Walle, *Phys. Rev. B: Condens. Matter Mater. Phys.*, 2010, **81**, 085212.

11 A. K. Chandiran, M. Abdi-Jalebi, M. K. Nazeeruddin and M. Grazel, *ACS Nano*, 2014, **8**, 2261–2268.

12 P. Tiwana, P. Docampo, M. B. Johnston, H. J. Snaith and L. M. Herz, *ACS Nano*, 2011, **5**, 5158–5166.

13 C. Fonstad and R. Rediker, *J. Appl. Phys.*, 1971, **42**, 2911–2918.

14 V. Stevanović, S. Lany, D. S. Ginley, W. Tumas and A. Zunger, *Phys. Chem. Chem. Phys.*, 2014, **16**, 3706–3714.

15 W.-J. Yin, S. Chen, J.-H. Yang, X.-G. Gong, Y. Yan and S.-H. Wei, *Appl. Phys. Lett.*, 2010, **96**(22), 221901.

16 Z. Kerrami, A. Sibari, O. Mounkachi, A. Benyoussef and M. Benaissa, *Int. J. Hydrogen Energy*, 2020, **45**, 11035–11039.

17 W. Zhou, Y. Liu, Y. Yang and P. Wu, *J. Phys. Chem. C*, 2014, **118**, 6448–6453.

18 W. Serbout, F. Bensouici, O. Meglali, S. Iaiche, M. Bououdina, S. Bellucci and M. Humayun, *Environ. Sci. Pollut. Res.*, 2023, **30**, 85792–85802.

19 P. Hohenberg and W. Kohn, *Phys. Rev.*, 1964, **136**, B864.

20 W. Kohn and L. J. Sham, *Phys. Rev.*, 1965, **140**, A1133.

21 G. Kresse and J. Hafner, *J. Phys.: Condens. Matter*, 1994, **6**, 8245.

22 G. Kresse and J. Furthmüller, *Phys. Rev. B: Condens. Matter Mater. Phys.*, 1996, **54**, 11169.

23 G. Kresse and J. Furthmüller, *Comput. Mater. Sci.*, 1996, **6**, 15–50.

24 J. P. Perdew, K. Burke and M. Ernzerhof, *Phys. Rev. Lett.*, 1996, **77**, 3865.

25 H. J. Monkhorst and J. D. Pack, *Phys. Rev. B*, 1976, **13**, 5188.

26 J. Paier, M. Marsman, K. Hummer, G. Kresse, I. C. Gerber and J. G. Ángyán, *J. Chem. Phys.*, 2006, **124**(15), 154709.

27 A. Togo and I. Tanaka, *Scr. Mater.*, 2015, **108**, 1–5.

28 V. I. Anisimov, F. Aryasetiawan and A. Lichtenstein, *J. Phys.: Condens. Matter*, 1997, **9**, 767.

29 S. L. Dudarev, G. A. Botton, S. Y. Savrasov, C. Humphreys and A. P. Sutton, *Phys. Rev. B: Condens. Matter Mater. Phys.*, 1998, **57**, 1505.

30 V. Wang, N. Xu, J.-C. Liu, G. Tang and W.-T. Geng, *Comput. Phys. Commun.*, 2021, **267**, 108033.

31 K. Momma and F. Izumi, *atelier de diffraction sur poudre Seventh Canadian Powder Diffraction Workshop*, 2006, p. 106.

32 F. Birch, *Phys. Rev.*, 1947, **71**, 809.

33 G. R. Portugal, G. G. Barbosa and J. T. Arantes, *Langmuir*, 2021, **37**, 4493–4503.

34 S. Zhang, H. Xiao, S. Peng, G. Yang, Z. Liu, X. Zu, S. Li, D. Singh, L. Martin and L. Qiao, *Phys. Rev. Appl.*, 2018, **10**, 044004.

35 R. Hill, *Proc. Phys. Soc., London, Sect. A*, 1952, **65**, 349.

36 D. Chung and W. Buessem, *J. Appl. Phys.*, 1968, **39**, 2777–2782.

37 E. E. Whiting, *J. Quant. Spectrosc. Radiat. Transfer*, 1968, **8**, 1379–1384.

38 S. Pugh, *J. Sci.*, 1954, **45**, 10–1080.

39 I. N. Frantsevich, *Reference book*, 1982.

40 M. Fine, L. Brown and H. Marcus, *Scr. Metall.*, 1984, **18**, 951–956.

41 M. Jiang, J. Zheng, H. Xiao, Z. Liu and X. Zu, *Sci. Rep.*, 2017, **7**, 9344.

42 J. Haines and J. Léger, *Phys. Rev. B: Condens. Matter Mater. Phys.*, 1997, **55**, 11144.

43 J. Pascual, J. Camassel and H. Mathieu, *Phys. Rev. B*, 1978, **18**, 5606.

44 Y. Tezuka, S. Shin, T. Ishii, T. Ejima, S. Suzuki and S. Sato, *J. Phys. Soc. Jpn.*, 1994, **63**, 347–357.

45 A. D. Becke and K. E. Edgecombe, *J. Chem. Phys.*, 1990, **92**, 5397–5403.

46 J. Zhang, P. Zhou, J. Liu and J. Yu, *Phys. Chem. Chem. Phys.*, 2014, **16**, 20382–20386.

47 K. J. Button, C. G. Fonstad and W. Dreybrodt, *Phys. Rev. B*, 1971, **4**, 4539.

48 R. G. Breckenridge and W. R. Hosler, *Phys. Rev.*, 1953, **91**, 793.

49 V. Celik, *Phys. B*, 2021, **619**, 413236.

50 A. Schleife, J. Varley, F. Fuchs, C. Rödl, F. Bechstedt, P. Rinke, A. Janotti and C. Van de Walle, *Phys. Rev. B: Condens. Matter Mater. Phys.*, 2011, **83**, 035116.

51 W. Yu, D. Xu and T. Peng, *J. Mater. Chem. A*, 2015, **3**, 19936–19947.

52 R. G. Pearson, *Inorg. Chem.*, 1988, **27**, 734–740.

This journal is © the Owner Societies 2025

Phys. Chem. Chem. Phys., 2025, **27**, 1284–1297 | 1297